1   **REVISION 1**

2   **TITLE**

3   **3T-PHLOGOPITE FROM KASENYI KAMAFUGITE (SW UGANDA):**

4   **EPMA, XPS, FTIR AND SCXRD STUDY**

5

6   Emanuela Schingaro, Maria Lacalamita, Fernando Scordari, Ernesto Mesto

7

8   Dipartimento di Scienze della Terra e Geoambientali, Università degli Studi di Bari,

9   via E. Orabona 4, I-70125 Bari, Italy

10

11

12

13
14
15
16
17
18
19
20
21
22
23
24
25
26
27
28
29
30   submitted to: *American Mineralogist*
31   word processor: *Word Microsoft Office 2003*
32   address of the corresponding author:
33   Prof. F. Scordari
34   Dipartimento di Scienze della Terra e Geoambientali, Università di Bari
35   Via Orabona 4, I-70125 Bari, Italy
36   Phone 0039-080-5442587
37   e-mail: fernando.scordari@uniba.it

ABSTRACT

38

39   A 3T mica polytype from Kasenyi (south west Uganda) kamafugite was studied by

40   Electron Probe Microanalysis (EPMA), Single Crystal X-ray Diffraction (SCXRD), micro-Fourier

41   Transform Infrared Spectoscopy (FTIR) and X-ray Photoelectron Spectroscopy (XPS) in order to

42   characterize its crystal chemistry and the relationships with phlogopites from the same rock but

43   showing different stacking sequence and, subordinately, to get insights into factors affecting

44   polytypism in ugandan phlogopites. EPMA data gave: SiO_2 = 38.7(2), Al_2O_3 = 13.08(9), MgO =

45   20.4(2), TiO_2 = 4.8(1), MnO = 0.03(3), FeO_{tot} = 5.51(9), Cr_2O_3 = 0.90(7), NiO = 0.11(5), SrO =

46   0.03(3), ZnO = 0.04(3), ZrO_2 = 0.01(2), K_2O = 9.64(5), Na_2O = 0.29(1), BaO = 0.15(5), F = 0.13(5)

47   and Cl = 0.01(1) wt%. The analysed sample may be classified as a Ti-rich phlogopite.

48   X-ray photoelectron spectroscopy provided Fe^{3+}/Fe^{2+} and O^{2-}/OH equal to ~ 0.75 and 7.14,

49   respectively, which are in agreement with the results of previous Mössbauer investigation on the

50   BU1 phlogopites from the same rock and with the structural formula of the studied crystal. Infrared

51   spectra showed, in the OH^- stretching region (~ 3740-3600 cm^{-1} cm^{-1}), a shoulder at ~ 3660 cm^{-1}

52   which is assigned to $MgMgFe^{3+}-OH^--K-O^{2-}$ local configurations. No evidences of vacancy

53   substitutions were observed.

54   Single crystal X-ray refinement using anisotropic displacement parameters was performed

55   in the $P3_112$ space group and converged to R_1 = 4.34 and wR_2 = 3.33 %. Unit cell parameters are: a

56   = b = 5.3235(3) and c = 30.188(2) Å. Geometrical and chemical considerations point to a disordered

57   cation distribution over T1 and T2 tetrahedral sites, whereas partial cation ordering characterizes the

58   octahedral sites with high charge cations preferentially located on M2 and M3, as expected.

59   Tetrahedral bond lengths distortion and angle variances parameters evidence more distorted

60   polyhedra in 3T polytype than those found in coexisting 1M and 2M_1 polytypes.

61   Finally, the overall crystal chemical features indicates the occurrence in the studied

62   sample of the following substitution mechanisms: Ti-oxy [$^{VI}M^{2+}$ + 2 $(OH)^-$ $\leftrightarrow$ $^{VI}Ti^{4+}$ + 2 (O^{2-}) +

63     $H_2\uparrow$] and Al, Fe^{3+}, Cr-oxy [$^{VI}M^{2+}$ + $(OH)^-$ $\leftrightarrow$ $^{VI}M^{3+}$ + O^{2-} + ½ $(H_2)\uparrow$]; Al, Fe^{3+}-Tschermak [$^{VI}M^{2+}$ +

64    $^{IV}Si^{4+} \leftrightarrow ^{VI}(Al^{3+}, Fe^{3+}) + ^{IV}Al^{3+}]; {}^{XII}K^+ + {}^{IV}Al^{3+} \leftrightarrow {}^{IV}Si^{4+} + {}^{XII}$; tetraferriphlogopite [$^{IV}Fe^{3+} \leftrightarrow$

65   ^{IV}Al].

66

67   **Keywords:** 3T-phlogopite, SCXRD, EPMA, FTIR, XPS, crystal chemistry, cation partitioning.

68

69   **INTRODUCTION**

70   1M, 2M_1 and 3T are the most common MDO mica polytypes classified as "Subfamily A

71   polytype" on the basis of successive layer rotation of 2$n \times 60°$ (with $n = 0$ for 1M, $n = 1$ and 2 for

72   2M_1 and $n = 1$ or 2 for 3T, Nespolo 1999; Ferrari and Ivaldi 2002). Among these, the 1M and 2M_1

73   are the most abundant polytypes in trioctahedral and dioctahedral micas, respectively, whereas the

74   3T polytype is very frequently occurring in dioctahedral micas (see Sassi et al. 2010 and references

75   therein). The total number of 3 layers polytypes, derived by Ross et al. (1966) is six, out of which

76   only two belong to the subfamily A. They are indicated as 3T[222] and 3Tc_1[02$\overline{2}$] in RTW notation

77   (Ross et al. 1966) and can be distinguished from their symmetry (3T has space group $P3_{1,2}12$

78   whereas 3Tc_1 has space group $C\overline{1}$, see also Takeda and Ross 1995). The characterization of mica

79   polytypes is complicated by the fact that it may not be easy to distinguish between true polytypes

80   and twinning that simulate a polytype with longer period, an issue know as "apparent polytypism"

81   (Nespolo 1999 and references therein). Two cases of apparent 3T polytypes (really due to 1M

82   polytypes twinned by pseudo-merohedry, each twin being composed of three individual

83   components rotated by ±120° around c*) have been recently reported by Nespolo and Kuwahara

84   (2001) and Scordari et al. (2012a). However, although very rare, trioctahedral 3T polytype really

85   occurs. The first structure model of a 3T-phlogopite dates back to Hendricks and Jefferson (1939).

86   Sanadaga and Takéuki (1961) identified a 3T trioctahedral mica by the analysis of diffraction

87   intensities. Since then, most of the single crystals of 3T trioctahedral micas found in nature resulted

88   to be Li-rich, in particular to belong to muscovite-polylithionite-annite system. X-ray diffraction

89   studies were carried out on these mica samples in order to describe their structure and define their

90   cation partitioning (Brown 1978; Pavlishin et al. 1981; Weiss et al. 1993; Brigatti et al. 2003). On

91   considering average octahedral distances and refined scattering powers, it was argued that in most

92   cases cation distribution with M1 = M3 > M2 occurred. Differently, M2 > M1 > M3 was found in

93   the case of lepidolite of Brown (1978).

94   Brigatti et al. (2003) found tetrahedral cation ordering in Li-micas with Al preferentially

95   located in T2 site, with the only exception of one sample of lithian siderophyllite.

96   More recently, 3T Mg-rich annite has been revealed by TEM investigations as coexisting in

97   the same crystal with other polytypes (see Fregola et al. 2009), whereas Gatta et al. (2011) studied

98   the crystal chemistry and the elastic behavior of a 3T-phlogopite from Traversella (Valchiusella,

99   Turin, Western Alps). The latter authors found M1 > M2 > M3 and T1 = T2 on a geometrical (bond

100   distances) basis and compared their sample with literature phlogopites and phengites, highlighting

101   that the elastic properties of micas depend on both the crystal chemistry and the symmetry of

102   polytypes.

103   In the present work, a 3T phlogopite from Kasenyi kamafugitic rock, SW Uganda, has been

104   investigated by integrating single crystal X-ray diffraction results (SCXRD) and electron probe

105   micro analyses (EPMA) with micro-Fourier transform infrared (micro-FTIR) and X-ray

106   photoelectron spectroscopy (XPS) inferences, in order to: 1) study in depth its crystal chemical

107   peculiarities; 2) shed light on similarities and/or differences between the 3T- and the 1M- and 2M_1-

108   micas from the same rock which were recently reported in the literature (see Lacalamita et al.

109   2012).

110   After Gatta et al. (2011), this is the second accurate X-ray structural study on a 3T mica of

111   the phlogopite-annite solid solution. All the analyses were carried out at ambient conditions. The

112   studied sample was collected from the ugandan melilitite bomb ("BU1" rock sample, see Mugnai

113   2003 and Stoppa et al. 2003) of Bunyampaka maar (Kasenyi field, south west Uganda).

114

115

116   **EXPERIMENTAL**

117   **Chemical analyses**

118   Electron probe microanalysis was performed on the (001) cleavage surface of the sample

119   pasted with graphite glue to a graphite base. A JEOL JXA-8200 electron microprobe operating at 15

120   kV accelerating voltage, 5 nA sample current, ~ 1 μm spot size and 40 s counting time was used. F,

121   Na, K, Ba, Cl, Ti, Cr, Mn, Ni, Sr, Zn, Zr were measured in wavelength dispersive spectrometry

122   (WDS) mode whereas Si, Al, Mg and Fe were quantified by energy dispersive spectrometry (EDS)

123   mode. The used standards were: grossular (Si-Al), olivine (Mg), omphacite (Na), ilmenite (Ti),

124   rhodonite (Mn), K-feldspar (K), Cr pure (Cr), fayalite (Fe), sanbornite (Ba), apatite (F), celestine

125   (Sr), nickeline (Ni), scapolite (Cl), rhodonite (Zn), zircon (Zr). A Phi-Rho-Z routine was employed

126   for the conversion from X-ray counts to oxide weight percentages (wt%).

127   The composition of ten spots was determined to check for the chemical zoning of the

128   analysed sample; the average composition is reported in Table 1, where it is compared with

129   representative analyses of coexisting $1M$ and $2M_1$ polytypes (Lacalamita et al 2012).

130

131   **Spectroscopic analyses**

132   X-ray photoelectron analysis was obtained by means of a Thermo VG Theta Probe X-ray

133   photoelectron spectrometer equipped with a microspot monochromatized Al Kα source. Before the

134   measurement, the investigated mica crystal was exfoliated inside the pre-vacuum chamber of the

135   XPS spectrometer under N_2 atmosphere. On the freshly cleaved crystal surface, both survey and

136   high-resolution spectra were acquired in fixed analyser transmission mode with pass energies of

137   150 and 100 eV, respectively. The acquired spectra were energy referenced to the aliphatic

138   component of C$1s$ signal having a binding energy BE = 284.8 eV. A curve fitting analysis of the

139   Fe$2p$ and O$1s$ narrow spectra was performed using a Gaussian - Lorentzian product function curves

140   as fitting functions (Ansell et al. 1979; Sherwood 1990). The results are shown in Figures 1, 2.

141   Infrared measurement was performed with a Nicolet Avatar FTIR spectrometer equipped

142   with a Continuum microscope, a MCT nitrogen-cooled detector and a KBr beamsplitter. An

143   unpolarized spectrum was collected in the range 4000-550 cm^{-1} with 4 cm^{-1} spectral resolution and

144   averaging 128 scans. The analysis was carried out with the crystal fixed to a glass fibre and laid on

145   the cleavage plane. The OH^- stretching region of the spectrum is illustrated in Figure 3 and

146   discussed in the **Chemical composition** section.

147

148   **Single crystal X-ray diffraction**

149   Structural determination was carried out with a Bruker AXS X8 APEXII automated

150   diffractometer equipped with a four-circle Kappa goniometer, a CCD detector, and a

151   monochromatized Mo$K\alpha$ ($\lambda = 0.7107$ Å) radiation. Operating conditions were: 50 kV and 30 mA,

152   crystal-to-detector distance of 40 mm. To check the crystal diffraction quality, preliminarily three

153   sets of 12 frames were acquired with 0.5° ω rotation and 10 s exposure time. The collection strategy

154   was optimized with the COSMO program in the APEX2 suite package (Bruker 2003a) and the

155   entire Ewald sphere was recorded by a combination of several ω and ϕ rotation sets, with 1.0° scan

156   width and 10 s per frame exposure time. The SAINT package was used for the extraction of the

157   reflection intensities and for the correction of the Lorentz-polarization (Bruker 2003b). The

158   SADABS software provided for a semi-empirical absorption correction (Sheldrick 2003). The

159   XPREP software assisted in the determination of the space group and in the calculation of the

160   intensity statistics.

161   The structure refinement was performed using the program CRYSTALS (Betteridge et al.

162   2003) in space group $P3_112$ and starting from the positional parameters of the lithian siderophyllite

163   from Pikes Peak batholith (Brigatti et al. 2003). Reflections with $I > 3\sigma(I)$ were considered as

164   observed and the refined parameters were: scale factor, atomic positions, cation occupancies, and

165   anisotropic atomic displacement parameters. Fully ionized scattering factors were used for

166   octahedral and interlayer sites and mixed scattering factors were employed for anion sites (O/O^{2-})

167   and for tetrahedral sites (Si/Si^{4+}), following Hawthorne et al. (1995). Full occupancy constraints

168   were used to fit the experimental electron density at octahedral sites, where Mg versus Fe were

169   refined, with Mg representing Mg + Al and Fe representing Fe + Ti + Cr scattering species.

170   Appropriate restraints (Watkin 1994) were used so that interlayer and tetrahedral site occupancy

171   factors could assume values greater or less than 1. Specifically, restraint on tetrahedral occupancy

172   allowed a better fit to the total scattering power at tetrahedral sites, where, due to the small

173   difference between their scattering curves, no least square refinement of Al versus Si was

174   attempted.

175   Crystal data, data-collection parameters and summary data about the structure refinement

176   are listed in Table 2 whereas final atomic coordinates, site occupancies, and isotropic and

177   anisotropic displacement parameters are reported in Table 3. Relevant cation-anion bond lengths,

178   mean atomic numbers and mean distances as determined by chemical analysis are given in Table 4.

179   The tetrahedral and octahedral cation partition is reported in Table 5. The distortion parameters

180   commonly used in crystal chemical studies on micas are listed in Table 6.

181

182   **RESULTS**

183   **Chemical composition**

184   The low coefficient of variation (CV, generally below 2%) associated to the weight oxides

185   of the main elements (SiO_2, Al_2O_3, MgO, FeO, TiO_2, K_2O) suggest that the single crystal analysed

186   is homogeneous, i.e. not chemically zoned (Table 1). It is a Ti-rich phlogopite, with composition

187   very close to those of other BU1 phlogopites showing $1M$ and $2M_1$ stacking sequences (see Table

188   1).

189   In the wide-scan X-ray photoelectron spectrum (see Figure 1), the expected peaks relevant

190   to the principal mica components (Si, Al, Mg, O and K) are observed. In the narrow scans of $Si2p$,

191    $K2p$, $Al2p$ and $Ti2p$ (not shown), the signals of $Si2p$, $Al2p$, $K2p_{3/2}$ and $Ti2p_{3/2}$ were used to derive

192   their binding energies: 101.6±0.1, 73.01±0.1, 293.2±0.1 and 548.78±0.1 eV, respectively. These

193   values are in agreement with those expected in silicate minerals. The narrow spectrum in the Fe$2p$

194   region (Figure 2a) of the 3T studied mica evidences the Fe$2p_{3/2}$ photoemission peak at a 709.8±0.1

195   eV binding energy. The curve fit of the Fe$2p$ region (after Shirley background subtraction) was

196   carried out following the Aronniemi et al. (2005) method in order to define the Fe oxidation states

197   of the studied sample. The Fe$2p_{3/2}$ peak was found to consist of three contributions ascribed to Fe^{2+}

198   (709.8±0.1eV), Fe^{3+} (711.1±0.1 eV) and Fe$_{shake-up}$ (713.9±0.1 eV). The full width at half maximum

199   values were 2.66, 3.85 and 4.00 eV for each component, respectively. The Fe^{3+}/Fe^{2+} area ratio

200   resulted to be ~ 0.75 which is in agreement with the Mössbauer results (^{IV}Fe^{3+} = 19(1) %, ^{VI}Fe^{2+} =

201   58(1) %, ^{VI}Fe^{3+} = 23(1) %, see Lacalamita et al. 2012) and the structural formula proposed for the

202   studied crystal (see the **Discussion and Conclusions** section below).

203   In Figure 2b, the narrow scan measured on the O$1s$ region is reported. The O$1s$ peak

204   resulted to be asymmetric and was fitted with two components at 531.4±0.1 and 532.9±0.1eV

205   binding energy values with equal full width at half maximum (2.46 eV). The first binding energy

206   value is typical of the oxygen (O^{2-}) in inorganic oxide such as Al$_2$O$_3$ (Takagi-Kawai et al. 1980), the

207   second one is characteristic of both OH$^-$ groups (Purvis et al. 2000) and adsorbed H$_2$O. However,

208   although H$_2$O is easily adsorbed on the surface of the inorganic samples, physically absorbed H$_2$O

209   is easily desorbed under the ultrahigh vacuum condition of the XPS system (Yu et al. 2003).

210   For such a reason, the hydrogenated group on the surface of the crystal sample may be

211   attributed to the structural hydroxyl of the studied mica. Despite of the interferences due to the

212   oxygen bond to the adventitious carbon, the O^{2-}/OH$^-$ area ratio was found to be 7.14, in good

213   agreement with that (~ 8) derived from the structural formula of the studied crystal (see the

214   **Discussion and Conclusions** section below).

215   The results of FTIR investigation on the BU1_13 crystal are shown in Figure 3. Specifically,

216   the infrared absorption in the OH$^-$-stretching region (~ 3740-3600 cm^{-1}) for the studied 3T-BU1

217   sample is shown in comparison to those of the rock coexisting 1M- and 2M_1-polytypes which were

218   very recently investigated (see Lacalamita et al. 2012). The IR absorption signals are very similar,

219   as expected being the 1M-, 2M_1- and 3T-BU1 micas chemically homogeneous. In addition, the OH$^-$

220   stretching spectra of the analysed samples are substantially alike to those reported in the literature

221   for other phlogopite affected by oxy-type substitutions (see Lacalamita et al. 2011; Scordari et al.

222   2006, 2012b). Figure 3 reveals the shoulder at 3660 cm^{-1}, ascribable to MgMgFe^{3+}-OH$^-$-K-O^{2-} local

223   configurations (Redhammer et al. 2000; Scordari et al. 2006; Lacalamita et al. 2011), whereas there

224   is no evidence of bands at 3620 and 3535 cm^{-1}, due to Al^{3+}Al^{3+}[]-OH$^-$ and Fe^{3+}Fe^{3+}[]-OH$^-$

225   arrangements (Libowitzky and Beran 2004; Scordari et al. 2008). It is concluded that the BU1_13

226   crystal, likewise the 1M- and 2M_1-BU1 samples, is affected by Fe^{3+}-oxy substitution mechanism

227   (^{VI}M^{2+} + (OH)$^-$ ↔ ^{VI}M^{3+} + O^{2-} + ½ (H$_2$)↑) and that vacancy substitutions (3^{VI}M^{2+} ↔ 2^{VI}M^{3+} + ^{VI}□,

228   with M^{3+} = Al^{3+}, Fe^{3+}, Cr^{3+}) do not affect the sample.

229

230   **Symmetry of the diffraction pattern**

231   The occurrence of reflections having both (h - k) = 3n and (k + l) ≠ 3n suggests that the

232   studied crystal was not a polysynthetic twin of the 1M polytype (see Güven and Burnham 1967 and

233   the section below). In addition, the systematic absences for (00l) reflections with l ≠ 3n indicated

234   the presence of a threefold screw axis parallel to c. The symmetry of the diffraction pattern is

235   illustrated in Figure 4a, b, c, d that shows reconstructed hk0, hk2, 0kl and 1kl precession images.

236   The hexagonal symmetry visible in Figure 4a is due to the two-dimensional orthohexagonal cell

237   typical of micas. However, in Figure 4b the real trigonal symmetry is more evident. On Figure 4c an

238   analysis of the lattice rows of the diffraction pattern, useful to identify the stacking sequence of

239   mica polytypes, has been accomplished following Nespolo et al. (1997): the S rows (h = 3n, k = 3n)

240   are "family reflections" and cannot be used to identify the polytype; the X-rows (k ≠ 3n) are "non-

241   family" reflections and permit the identification of the stacking period. In Figure 4c it is apparent

242   that in the 0.1 Å^{-1} period along X rows there are three reflections, suggesting that the sample is a 3-

243   layer polytype. Further details on this issue are given below. In Figure 4d the 1kl reciprocal plane

244   confirms the symmetry observed in Figure 4c.

245   The above observations result in possible space groups $P3_112$ or $P3_212$.
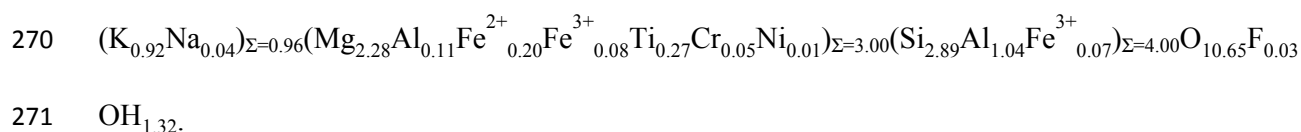
246

247   **Structural analysis**

248   The first step of the structural analysis was to check whether the 3-layer crystal was instead

249   a $1M$ polytypes twinned by pseudo-merohedry, composed of three individual components rotated

250   by $\pm120°$ around c*. The unit cell of the $1M$ individual and the orientation matrices of the other

251   components of the twin were obtained using the program CELL_NOW (Bruker 2008) and the

252   relevant twin laws were employed in the structure refinement. However, the refinement did not

253   converge. Therefore, an anisotropic structure refinement was carried out using the space group

254    $P3_112$. The analysis of the absolute configuration was performed employing a routine recently

255   implemented in CRYSTALS (Thompson and Watkin 2011). The refinement converged at $R_1 =$

256   6.59, $wR_2 = 6.31\%$, with Flack parameter = 0.31(40) and Hooft parameter = 0.53(13). It is

257   concluded that the absolute structure cannot be reliably determined, and that possibly the sample is

258   a racemic twin. However, an attempt to introduce the twin law into the structure refinement yielded

259   the same R factors as above, whereas the scale factors for the twin components refined to 0.7(4) and

260   0.3(4). This means that the exact twin ratio is poorly determined. In addition this refinement leads

261   to octahedral mean atomic numbers $e^-_{(M1)} = 14.34$, $e^-_{(M2)} = 15.12$, $e^-_{(M3)} = 14.81$, that are not

262   significantly different from those obtained from the no twin refinement. At this stage it was clear

263   that there was no information into the Friedel pairs, so they were merged and the refinement redone.

264   It converged at $R_1 = 4.34\%$ and $wR_2 = 3.33\%$ with negligible residual electron density in the

265   difference Fourier map (see Table 2).

266

267   **DISCUSSION AND CONCLUSIONS**

268   The combination of results from multiple techniques led to the following final structural

269   formula, based on $[O_{12-(x+y+z)} (OH)_x Cl_y F_z]$, for the study sample:

270     $(K_{0.92}Na_{0.04})_{\Sigma=0.96}(Mg_{2.28}Al_{0.11}Fe^{2+}_{0.20}Fe^{3+}_{0.08}Ti_{0.27}Cr_{0.05}Ni_{0.01})_{\Sigma=3.00}(Si_{2.89}Al_{1.04}Fe^{3+}_{0.07})_{\Sigma=4.00}O_{10.65}F_{0.03}$

271     $OH_{1.32}$.

272   Because the chemical composition among the coexisting $1M$, $2M_1$ and $3T$ polytypes of

273   Kasenyi phlogopite is similar (see comparison in Table 1), the H_2O content geometrically estimated

274   for the $1M$- and $2M_1$-BU1 coexisting micas was adopted as starting value for the formula

275   calculation of the study sample. In addition, the near surface Fe^{3+}/Fe^{2+} ratio, as determined by XPS

276   analysis (see above) was found to be consistent with the results of previous room-temperature

277   Mössbauer spectroscopy measurement (Lacalamita et al. 2012). This indicates that near surface

278   features in our sample are close to the bulk ones and that, thanks to the remarkable intergranular

279   homogeneity (see Table 1), the Fe^{3+}/Fe^{2+} ratio from one single crystal (this work) is similar to that

280   obtained from many powdered single crystals (Mössbauer analysis). Last but not least, from a

281   crystal chemical viewpoint, once the water content is given (measured or estimated), if the average

282   Fe^{3+}/Fe^{2+} were too much different from that of the individual single crystals, a bad agreement

283   between observed and calculated mean atomic numbers at octahedral sites (i.e. the $e^-_{(M1+M2+M3)\,X\text{-ref}}$

284   and $e^-_{(M1+M2+M3)\,EPMA}$) would result (see Ottolini et al. 2012). In our case, the difference between

285   observed and calculated m.a.n.'s for octahedral sites is 1.19 e^-, i.e. 0.40 e^- per site (Table 4).

286   The above structural formula is balanced on the basis of the following substitutions: Ti-oxy

287     $[^{VI}M^{2+} + 2\,(OH)^- \leftrightarrow {}^{VI}Ti^{4+} + 2\,(O^{2-}) + H_2\uparrow]$; Al, Fe^{3+}, Cr-oxy $[^{VI}M^{2+} + OH^- \leftrightarrow {}^{VI}M^{3+} + O^{2-} + \frac{1}{2}$

288     $(H_2)\uparrow]$; Al, Fe^{3+}-Tschermak $[^{VI}M^{2+} + {}^{IV}Si^{4+} \leftrightarrow {}^{VI}(Al^{3+}, Fe^{3+}) + {}^{IV}Al^{3+}]$; tetraferri-phlogopite

289     $[^{IV}Fe^{3+} \leftrightarrow {}^{IV}Al]$ and $^{XII}K^+ + {}^{IV}Al^{3+} \leftrightarrow {}^{IV}Si^{4+} + {}^{XII}\square$. Therefore, the sample can be classified as a Ti-

290   phlogopite with a minor tetraferriphlogopite content.

291   The chemical data are consistent with X-ray data, as testified not only by the good

292   agreement between X-ref and EPMA derived mean atomic numbers but also by a good match

293   between observed and calculated <T-O> and <M-O> distances (Table 4). In particular, the

294   calculated distances were determined from the molar fractions measured from EPMA and using

295   radii from Shannon (1976) and mean anion radii from Kogarko et al. (2005). For the study sample,

296   the cation partition that best fits with X-ray data is reported in Table 5. Note that the tetrahedral

297   sites are characterized by disorder, i.e. Si, Al and Fe^{3+} are equally partitioned over T1 and T2 sites

298   (see Table 5). This explains the close similarity between the <T1-O> and <T2-O> mean bond

299   distances and the T1 and T2 mean atomic numbers (e^-). It is noteworthy that $^{IV}Fe^{3+}$, estimated by

300   the formula <T-O> (Å) = $1.607 + 4.201 \cdot 10^{-2}$ Al $+ 7.68 \cdot 10^{-2}$ Fe (with Al and Fe in atoms per

301   formula unit) given in Brigatti and Guggenheim (2002), provides 0.08 atoms per formula unit

302   which compares well with the value estimated from Mössbauer spectroscopy. The average

303   octahedral distances (Table 4) in the $3T$ phlogopite are similar to those found for the $1M$ and $2M_1$

304   polytypes from the same BU1 rock (<M1-O> = 2.084 and 2.083 Å respectively, <M2-O> = 2.068

305   and 2.069 Å respectively, see Lacalamita et al 2012). The final octahedral cation distribution was

306   obtained by also considering that the so called "$Shift_{M2}$" parameter (see Table 6) is known to be

307   proportional to the oxy component (Lacalamita et al. 2011). In this case the parameter was

308   calculated for all the three M sites and indicated that high charged cations prefer M2 and M3 sites,

309   consistently with previous findings on Ti-phlogopites with different stacking sequences (Cesare et

310   al. 2003; Sassi et al. 2008; Lacalamita et al. 2012; Scordari et al 2012b). On the whole, however, the

311   sample studied here is homo-octahedral both from a geometrical (Weiss et al. 1985, 1992) and a

312   chemical (Ďurovíč 1994, see Table 4, 5) viewpoint.

313   Note also that the octahedral cation distribution in terms of m.a.n.'s is very similar in all three

314   coexisting polytypes (Table 5).

315   From a structural viewpoint, the refined unit cell parameters of the BU1_13 crystal are

316   slightly higher ($a = b = 5.3235(3)$, $c = 30.188(2)$ Å) than those of the $3T$ lithium micas ($a = b \sim$

317   5.29, $c \sim 29.82$ Å) but the c-parameter is lower than those of the literature $3T$-phlogopite ($a = b =$

318   5.3167(4), $c = 30.44(2)$ Å, Gatta et al. 2011). As commonly occurs in the dehydrogenated $1M$ and

319    $2M_1$ micas (Scordari et al. 2012b), also in the $3T$ mica polytype the increase of the high charge

320 cations (Al, Fe^{3+}, Ti, Cr) in the octahedral site is related to the decrease of the c lattice parameter

321 whereas its effect on the a and b cell parameters seems negligible (Figure 5).

322   In Figure 6 the variation of the in-plane rotation angle (α) versus the sum of high charge

323 octahedral cations is illustrated. In micas, notoriously the α angle helps to reduce the mismatch

324 between the lateral dimensions of the octahedral and tetrahedral sheets and is a function of the

325 tetrahedral, octahedral and anionic sites composition (Bailey 1984; Brigatti and Guggenheim 2002).

326 In Figure 6 the study sample plots in between the 3T-phlogopite from Traversella (Gatta et al. 2011)

327 and the other literature Li-rich 3T-micas. This can be explained considering that, with respect to the

328 latter samples, the 3T-BU1 mica is almost F-free. With respect to the phlogopite from Gatta et al.

329 (2011), the 3T-BU1 mica has a lower α parameter (7.54° versus 9.88°) because of the greatest oxy

330 component (O^{2-} = 0.65 vs. 0.00 atoms per formula unit for the study and the literature 3T-mica,

331 respectively). The anomalous behaviour of the lepidolite of Brown (1978), which departs from the

332 trends shown in this figure, may depend on the low quality of the structure refinement.

333   Over the whole dataset, the 3T-BU1 sample exhibits also the greatest values of the mean

334 tetrahedral bond length distortion (<BLD>$_T$ ~ 1.37) as shown in Figure 7. If compared with the

335 coexisting 1M- and 2M_1-BU1 polytypes recently studied by Lacalamita et al. (2012), the 3T mica

336 here analysed shows similar values of α parameter, thicknesses and volumes of polyhedra but

337 higher values of <BLD>$_T$ and tetrahedral angle variance, <TAV> parameters (see Table 6 and

338 Figures 6, 7). These results suggest that bond lengths in tetrahedra are more strained in 3T- with

339 respect to 1M- and 2M_1-BU1 polytypes.

340   Studies on the relative stability of polytypes indicate that the increase of pressure favours 3T

341 over 2M_1 in phengites (Curetti et al. 2006 and references therein). Gatta et al. (2011), instead,

342 conclude that 3T trioctahedral micas are slightly less stable than 1M as a function of pressure on the

343 basis of the calculation of the deformation energies (volume/p.f.u.). In our case, we find ~ 247 $Å^3$ in

344 all three polytypes, implying that, as expected, negligible energetic differences exist among 1M- ,

345 2M_1- and 3T-BU1 polytypes.

346   At the present state of our investigation on ugandan phlogopites, we can conclude that the

347     $1M$ and $2M_1$ stacking sequences are the most abundant (with a prevalence of the former) in the

348   Kasenyi BU1 rock of the present work, whereas the $3T$ is very subordinate. The coexistence of

349   different polytypes seems not due to crystal chemical factors (see Tables 1, 5), at least at the bulk

350   scale. On the other hand, when such compositional differences exists, they do not result into

351   different polytypic sequences, as found in a previous investigation on $2M_1$ ugandan phlogopites

352   from Bunyaruguru kamafugite (BU3 rock, Scordari et al. 2012b). Indeed in that case, two groups of

353   phlogopites were distinguished on the basis of the octahedral composition and on the extent of the

354   oxy-substitution component (Ti ~ 0.30 apfu, shift$_{M2}$ ~ 0.06 Å, O^{2-} ~ 10.80 apfu for group 1 and Ti ~

355   0.40 apfu, shift$_{M2}$ ~ 0.08 Å, O^{2-} ~ 11.00 apfu for group 2). However, only $2M_1$ polytypes formed in

356   that rock. The same conclusions may be reached when stacking induced distortion are taken into

357   considerations. In Lacalamita et al. (2012), the comparison between $1M$ and $2M_1$ polytypes from the

358   same kamafugite here considered, led to conclude that the stacking distortions induced at the

359   octahedral level (and evaluated as a relative shift of the upper and lower triads of octahedral

360   oxygens along the $\pm b$ directions with respect to the $1M$ octahedral sheet) did not influence the

361   stability of the $2M_1$ polytype. In the present work, our findings on the coexisting $3T$ crystal indicate

362   that the most pronounced distortions pertain to the tetrahedra in the $3T$ with respect to the $2M_1$ and

363     $1M$ polytype. Again, these are not due to the site chemistry but may be associated to different

364   geometric constraints that each unit-layer exerts over adjacent layers in the $3T$ stacking sequence,

365   and could explain the much rarer occurrence of the trigonal polytype with respect to the monoclinic

366   ones in the case of Kasenyi phlogopite. In our opinion, an interplay of other factors, like kinetics of

367   growth, fluctuations in the degree of supersaturation of the crystallization environment (see review

368   in Bozhilov et al. 2009) have played a role in modulating the effects of short range and long range

369   interactions responsible for the formation of the observed three coexisting basic polytypes.

370

371

379

380   **REFERENCES**

381   Ansell, R.O., Dickinson, T., Povey, A.F., and Sherwood, P.M.A (1979) X-ray photoelectron

382   spectroscopic studies of electrode surfaces using a new controlled transfer technique: Part II.

383   Results for a molybdenum electrode and the curve fitting procedure. Journal of Electroanalytical

384   Chemistry and Interfacial Electrochemistry, 98, 79-89.

385   Aronniemi, M., Sainio, J., and Lahtinen, J. (2005) Chemical state quantification of iron and

386   chromium oxides using XPS: the effect of the background subtraction method. Surface Science,

387   578, 108-123.

388   Bailey, S.W. (1984) Crystal chemistry of the true micas. In S.W. Baley, Ed., Micas, 13, 13–61.

389   Reviews in Mineralogy, Mineralogical Society of America, Chantilly, Virginia.

390   Balic Zunic, T. and Vickovic, I. (1996) IVTON- a program for the calculation of geometrical

391   aspects of crystal structures and some crystal chemical applications. Journal of Applied

392   Crystallography, 29, 305-306.

393   Betteridge, P.W., Carruthers, J.R., Cooper, R.I., Prout, K., and Watkin, D.J. (2003) Crystals version

394   12: software for guided crystal structure analysis. Journal of Applied Crystallography, 36, 1487.

395   Bozhilov, K.N., Xu, Z., Dobrzhinetskaya, L.F., Jin, Z.-M., and Green II, H.W. (2009) Cation-

396   deficient phlogopitic mica exsolution in diopside from garnet peridotite in SuLu, China. Lithos,

397   109, 304-313.

398   Brigatti, M.F. and Guggenheim, S. (2002) Mica crystal chemistry and the influence of pressure,

399   temperature, and solid solution on atomistic models. In A. Mottana, F.P. Sassi, J.B. Jr.

400   Thompson, and S. Guggenheim, Eds., Micas: Crystal Chemistry and Metamorphic Petrology, 46,

401   1–97. Reviews in Mineralogy and Geochemistry, Mineralogical Society of America and the

402   Geochemical Society, Chantilly, Virginia.

403   Brigatti, M.F., Kile, D.E., and Poppi, L. (2003) Crystal structure and chemistry of lithium-bearing

404   trioctahedral micas-3T. European Journal of Mineralogy, 15, 349-355.

405   Brown, B.E. (1978) The crystal structure of a 3T lepidolite. American Mineralogist, 63, 332-336.

406   Bruker (2003a) *APEX2*. Bruker AXS Inc., Madison, Wisconsin, USA.

407   Bruker (2003b) *SAINT*. Bruker AXS Inc., Madison, Wisconsin, USA.

408   Bruker (2008) *CELL_NOW* and *TWINABS*. Bruker AXS Inc., Madison, Wisconsin, USA.

409   Cesare, B., Cruciani, G., and Russo, U. (2003) Hydrogen deficiency in Ti-rich biotite from anatectic

410   metapelites (El Joyazo, SE Spain): Crystal-chemical aspects and implications for high-

411   temperature petrogenesis. American Mineralogist, 88, 583-595.

412   Curetti, N., Levy, D., Pavese, A., and Ivaldi, G. (2006) Elastic properties and stability of coexisting

413   3T and 2M_1 phengite polytypes. Physics and Chemistry of Minerals, 32, 670-678.

414   Donnay, G., Morimoto, N., Takeda, H., and Donnay, J.D.H. (1964a) Trioctahedral one-layer micas.

415   I. Crystal structure of a synthetic iron mica. Acta Crystallographica, 17, 1369–1373.

416   Donnay, G., Donnay, J.D.H., and Takeda, H. (1964b) Trioctahedral one-layer micas. II. Prediction

417   of the structure from composition and cell dimensions. Acta Crystallographica, 17, 1374–1381.

418   Ďurovíč, S. (1994) Classification of phyllosilicates according to the symmetry of their octahedral

419   sheets. Ceramics – Silikáty, 38, 81-84.

420   Ferraris, G. and Ivaldi, G. (2002) Structural features of micas. In A. Mottana, F.P. Sassi, J.B. Jr.

421   Thompson, and S. Guggenheim, Eds., Micas: Crystal Chemistry and Metamorphic Petrology, 46,

422   117-153. Reviews in Mineralogy and Geochemistry, Mineralogical Society of America and the

423   Geochemical Society, Chantilly, Virginia.

424   Fregola, R.A., Capitani, G., Scandale, E., and Ottolini, L. (2009) Chemical control of 3T stacking

425   order in a Li-poor biotite mica. American Mineralogist, 94, 334-344.

426   Gatta, G.D., Merlini, M., Rotiroti, N., Curetti, N., and Pavese, A. (2011) On the crystal chemistry

427   and elastic behavior of a phlogopite 3T. Physics and Chemistry of Minerals, 38, 655-664.

428   Güven, N. (1971) The crystal structure of 2M_1 phengite and 2M_1 muscovite. Zeitschrift für

429   Kristallographie, 134, 196–212.

430   Güven, N. and Burnham, C.W. (1967) The crystal structure of 3T muscovite. Zeitschrift für

431   Kristallographie, 125, 163–183.

432   Hawthorne, F.C., Ungaretti, L., and Oberti, R. (1995) Site populations in minerals: terminology and

433   presentation of results. Canadian Mineralogist, 33, 907-911.

434   Hazen, R.M. and Burnham, C.W. (1973) The Crystal Structures of One-Layer Phlogopite and

435   Annite. American Mineralogist, 58, 889–900.

436   Hendricks, S.B. and Jefferson, M.E. (1939) Polymorphism of the micas with optical measurements.

437   American Mineralogist, 24, 729-771.

438   Kogarko, L.N., Uvarova, Y.A., Sokolova, E., Hawthorne, F.C., Ottolini, L., and Grice, J.D. (2005)

439   Oxykinoshitalite, a new species of mica from Fernando-de-Noronha Island, Pernambuco, Brazil:

440   occurrence and crystal structure. Canadian Mineralogist, 43, 1501-1510.

441   Lacalamita, M., Schingaro, E., Scordari, F., Ventruti, G., Fabbrizio, A., and Pedrazzi, G. (2011)

442   Substitution mechanisms and implication on the estimate of water fugacity for Ti-phlogopite

443   from Mt. Vulture (Potenza, Italy). American Mineralogist, 96, 1381-1391.

444   Lacalamita, M., Mesto, E., Scordari, F., and Schingaro, E. (2012) Chemical and structural

445   comparison of 1M- and 2M_1-phlogopites coexsisting in the same Kasenyi kamafugitic rock (SW

446   Uganda). Physics and Chemistry of Minerals, 39, 601-611.

447   Libowitzky, E. and Beran, A. (2004) IR spectroscopic characterisation of hydrous species in

448   minerals. In A. Beran and E. Libowitzky, Eds., Spectroscopic methods in mineralogy, 6, 227-

449   280. EMU Notes in Mineralogy. Eötvös University Press, Budapest.

450 Mugnai, M. (2003) Il distretto vulcanico e geochimico delle province magmatiche di Toro Ankole e

451   Bufumbira (Uganda), 246 p. Degree thesis, University of Chieti, Italy.

452 Nespolo, M. (1999) Analysis of family reflections of OD mica polytypes, and its application to twin

453   identification. Mineralogical Journal, 21, 53-85.

454 Nespolo, M. and Kuwahara, Y. (2001) Apparent polytypism in the Ruiz Peak ferric phlogopite.

455   European Journal of Mineralogy, 13(6), 1047-1056.

456 Nespolo, M., Takeda, H., Ferraris, G., and Kogure, T. (1997) Composite twins of $1M$ mica:

457   derivation and identification. Mineralogical Journal, 19, 173-186.

458 Ottolini, L., Schingaro, E., and Scordari, F. (2012) Ceramics: Contribution of Secondary Ion Mass

459   Spectrometry (SIMS) to the Study of Crystal Chemistry of Mica Minerals. In M.S. Lee, Ed.,

460   Mass Spectrometry Handbook, 43, 1017-1060. Wiley Series on Pharmaceutical Science and

461   Bioteechnology: Practices, Applications, and Methods, J. Wiley & Sons, Inc., Hoboken, NJ,

462   USA.

463 Pavlishin, V.I., Semenova, T.F., and Rozhdestvenskaya, I.V. (1981) Protolithionite-$3T$: its structure,

464   typomorphism, and pratical significance. Mineralogicheskii Zhurnal, 1, 47-60.

465 Purvis, K.L., Lu, G., Schwartz, J., and Bernasek, S.L. (2000) Surface Characterization and

466   Modification of Indium Tin Oxide in Ultrahigh Vacuum. Journal of the American Chemical

467   Society, 122, 1808-1809.

468 Redhammer, G.J., Beran, A., Schneider, J., Amthauer, G., and Lottermoser, W. (2000)

469   Spectroscopic and structural properties of synthetic micas on the annite-siderophyllite binary:

470   Synthesis, crystal structure refinement, Mössbauer, and infrared spectroscopy. American

471   Mineralogist, 85, 449–465.

472 Renner, B. and Lehmann, G. (1986) Correlation of angular and bond length distortions in TO$_4$ units

473   in crystals. Zeitschrift für Kristallographie, 175, 43–59.

474 Robinson, K., Gibbs, G.V., and Ribbe, P.H. (1971) Quadratic Elongation: A Quantitative Measure

475   of Distortion in Coordination Polyhedra. Science, 172, 567–570.

476   Ross, M., Takeda, H., and Wones, D.R. (1966) Mica polytypes: Systematic description and

477   identification. Science, 151, 191-193.

478   Sadanaga, R. and Takeuchi, Y. (1961) Polysynthetic twinning of micas. Zeitschrift für

479   Kristallographie, 116, 406-429.

480   Sassi, R., Cruciani, G., Mazzoli, C., Nodari, L., and Craven, J. (2008) Multiple titanium

481   substitutions in biotites from high-grade metapelitic xenoliths (Euganean Hills, Italy): Complete

482   crystal chemistry and appraisal of petrologic control. American Mineralogist, 93, 339-350.

483   Sassi, R., Brigatti, M.F., Gomez-Pugnaire, M.T., Peruzzo, L., Tellini, F., and Sassi, F.P. (2010)

484   What drives the distribution in nature of $3T$ vs. $2M_1$ polytype in muscovite and phengites? A

485   general assessment based on new data from metamorphic and igneous granitoid rocks. American

486   Mineralogist, 95, 1182-1191.

487   Scordari, F., Ventruti, G., Sabato, A., Bellatreccia, F., Della Ventura, G., and Pedrazzi, G. (2006)

488   Ti-rich phlogopite from Mt. Vulture (Potenza, Italy) investigated by a multianalytical approach:

489   substitutional mechanisms and orientation of the OH dipoles. European Journal of Mineralogy,

490   18, 379-391.

491   Scordari, F., Schingaro, E., Ventruti, G., Lacalamita, M., and Ottolini, L. (2008) Red micas from

492   basal ignimbrites of Mt. Vulture (Italy): interlayer content appraisal by a multi-methodic

493   approach. Physics and Chemistry of Minerals, 35, 163-174.

494   Scordari, F., Schingaro, E., Ventruti, G., Nicotra, E., Viccaro, M., and Mazziotti Tagliani, S.

495   (2012a) Fluorphlogopite from Piano delle Concazze (Mt. Etna, Italy): crystal chemistry and

496   implications for the crystallization conditions. American Mineralogist, accepted.

497   Scordari, F., Schingaro, E., Lacalamita, M., Mesto, E. (2012b) Crystal chemistry of trioctahedral

498   micas-$2M_1$ from Bunyaruguru (SW Uganda) kamafugite. American Mineralogist, 97, 430-439.

499   Shannon, R.D. (1976) Revised effective ionic radii and systematic studies of interatomic distances

500   in halides and chalcogenides. Acta Crystallogaphica, A 32, 751–767.

501   Sheldrick, G.M. (2003) SADABS, Program for Empirical Absorption Correction of Area Detector

502   Data. University of Göttingen, Germany.

503   Sherwood, P.M.A. (1990) Appendix 3. In D. Briggs and M.P. Seah, Eds., Practical Surface

504   Analysis: Auger and X-ray Photoelectron Spectroscopy, 1, 555-586. ISBN-10: 0471920819.

505   ISBN-13: 978-0471920816.

506   Stoppa, F., Lloyd, F.E., and Rosatelli, G. (2003) CO_2 as the virtual propellant of carbonatite-

507   kamafugite conjugate pairs and the eruption of diatremic tuffisite. Periodico di Mineralogia, 72,

508   Special Issue Eurocarb, 1-18.

509   Takagi-Kawai, M., Soma, M., Onishi, T., and Tamaru, K. (1980) The absorption and the reaction of

510   NH_3 and NO_x on supported V_2O_5 catalysts: effect of supporting materials. Canadian Journal of

511   Chemistry, 58(20), 2132-2137.

512   Takeda, H. and Ross, M. (1995) Mica polytypism: Identification and origin. American

513   Mineralogist, 80, 715-724.

514   Thompson, A.L. and Watkin, D.J. (2011) *CRYSTALS* enhancements: absolute structure

515   determination. Journal of Applied Crystallography, 44, 1017-1022.

516   Toraya, H. (1981) Distortions of octahedra and octahedral sheets in 1*M* micas and the relation to

517   their stability. Zeitschrift für Kristallographie, 157, 173-190.

518   Watkin, D. (1994) Foundations of crystallography. Acta Crystallographica, A50, 411-434.

519   Weiss, Z., Rieder, M., Chmielová, M., and Krajíček, J. (1985) Geometry of the octahedral

520   coordination in micas: a review of refined structures. American Mineralogist, 70, 747-757.

521   Weiss, Z., Rieder, M., and Chmielová, M. (1992) Deformation of coordination polyhedra and their

522   sheets in phyllosilicates. European Journal of Mineralogy, 4, 665-682.

523   Weiss, Z., Rieder, M., Smrčok, L'U., Petříček, V., and Bailey, S.W. (1993) Refinement of the

524   crystal structures of two "protolithionites". European Journal of Mineralogy, 5, 493-502.

525   Yu, J.-G., Yu, H.-G., Cheng, B., Zhao, X.-J., Yu, J.C., and Ho, W.-K. (2003) The effect of

526   Calcination Temperature on the Surface Microstructure and Photocatalytic Activity of TiO_2 Thin

527   Films Prepared by Liquid Phase Deposition. The Journal of Physical Chemistry B, 107(50),

528   13871-13879.

529

530   **FIGURE CAPTIONS**

531   **FIGURE 1.** X-ray photoelectron spectroscopy wide-scan spectrum of BU1_13 crystal.

532   **FIGURE 2.** High-resolution photoelctron spectra of (**a**) Fe*2p* and (**b**) O*1s* regions for the studied

533   Bu1_13 crystal.

534   **FIGURE 3.** OH$^-$ stretching region in the FTIR spectrum of BU1_13 crystal. For comparison, the

535   spectra of coexisting 1*M*- and 2*M*$_1$-polytype are shown. The region of the MgMgFe^{3+}-OH$^-$-K-O^{2-}

536   band is highlighted.

537   **FIGURE 4.** Reconstructed precession images for the studied Bu1_13 crystal. **a)**, **b)**, **c)** and **d)**

538   represent the level *hk*0, *hk*2, *0kl* and 1*kl*, respectively.

539   **FIGURE 5.** Relation between the unit cell parameters and the sum of octahedral high charge

540   cations content (Al + Fe^{3+} + Cr + Ti). Symbols: solid symbol = Ti-rich phlogopite of this study

541   (BU1_13 sample); open symbols = literature 3*T* micas (triangle pointing downward: Brown 1978;

542   triangle pointing upward: Pavlishin et al. 1981; circle: Weiss et al. 1993; square: Brigatti et al.

543   2003; diamond = Gatta et al. 2011).

544   **FIGURE 6.** Plot of the in plane rotation angle, α parameter, vs. octahedral (Al + Fe^{3+} + Cr + Ti)

545   content. Symbols as in Figure 5. In addition, the x and circle with vertical line symbols indicate 1*M*-

546   and 2*M*$_1$-BU1 micas, respectively, from Lacalamita et al. (2012).

547   **FIGURE 7.** Plot of mean tetrahedral bond length distortion (<BLD>$_T$ parameter) vs. tetrahedral (Al

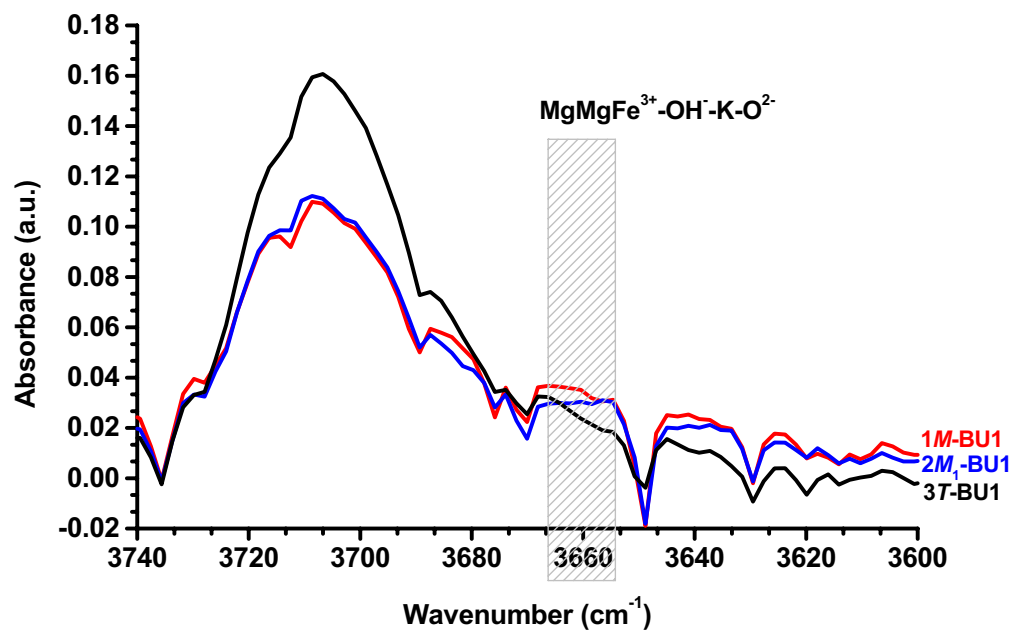548   + Fe^{3+}) content. Symbols as in Figure 6.
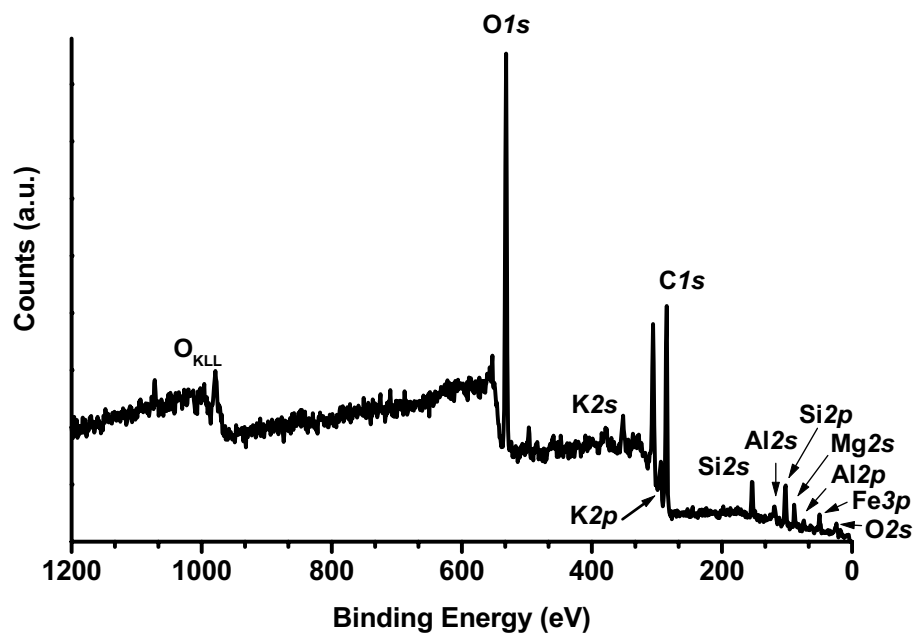
Figure 1
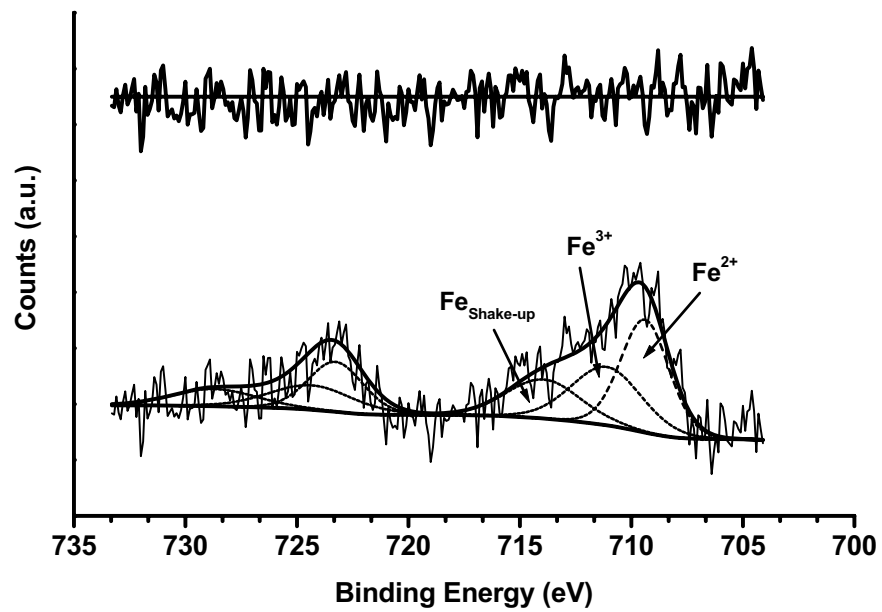
Figure 2a
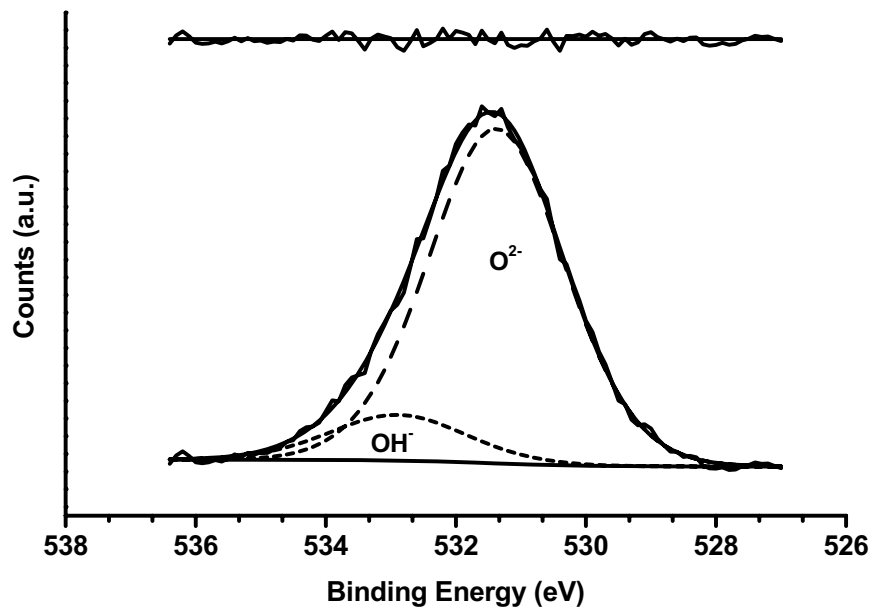
Figure 2b

Figure 3
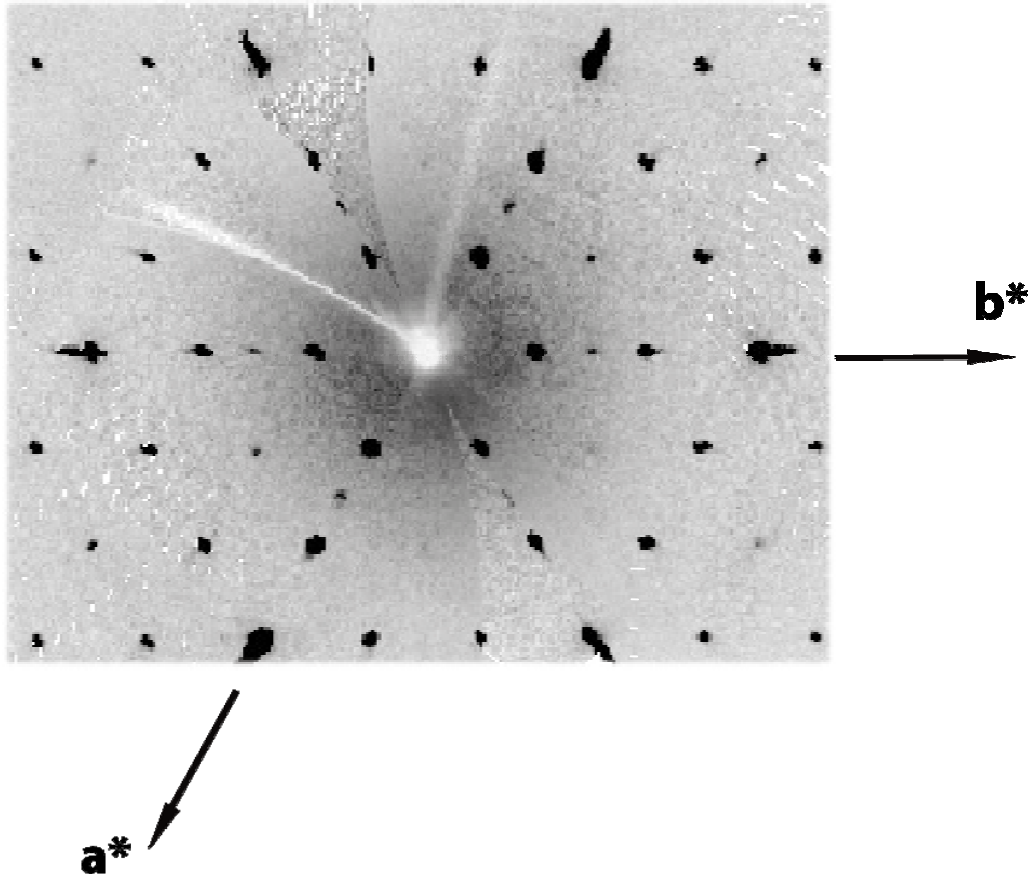
Figure 4a
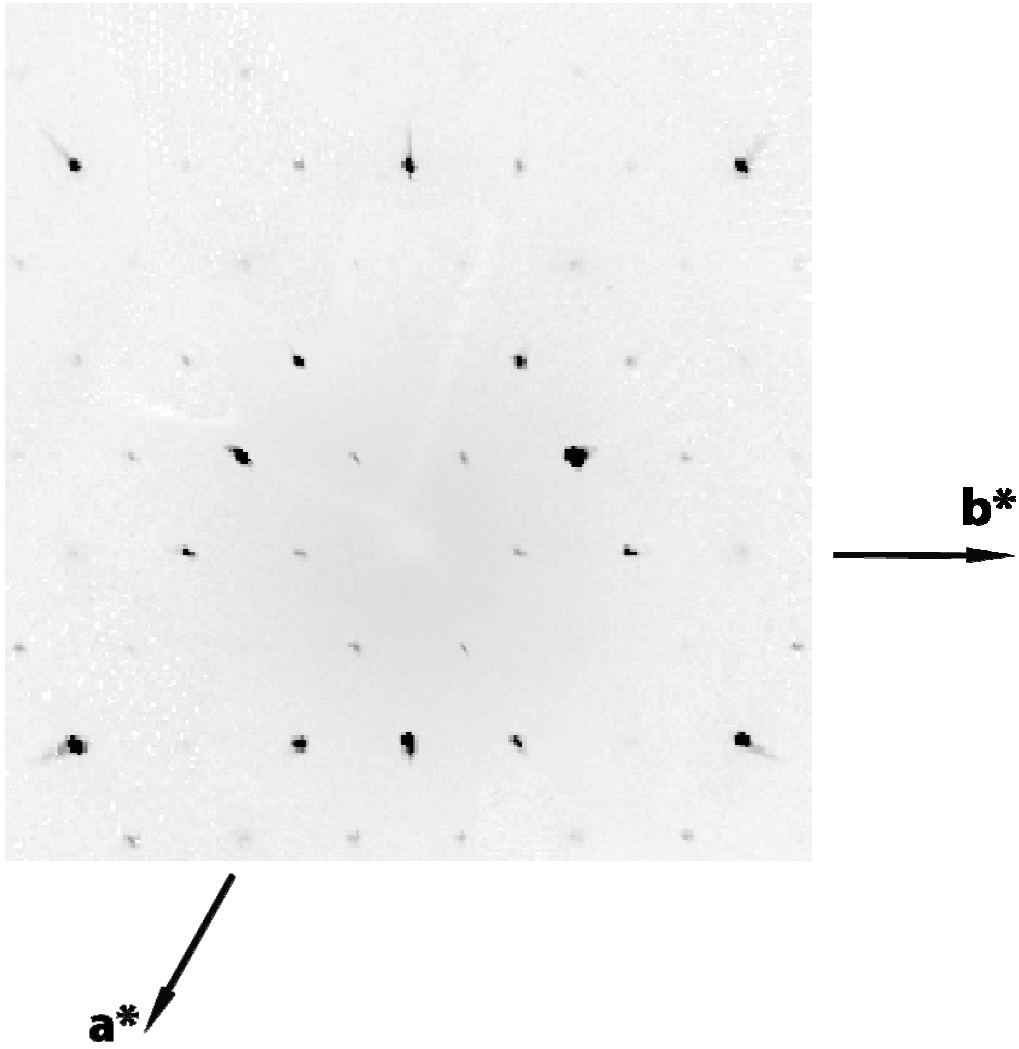
Figure 4b

Figure 4c

X X S X X S X X

c*

b*
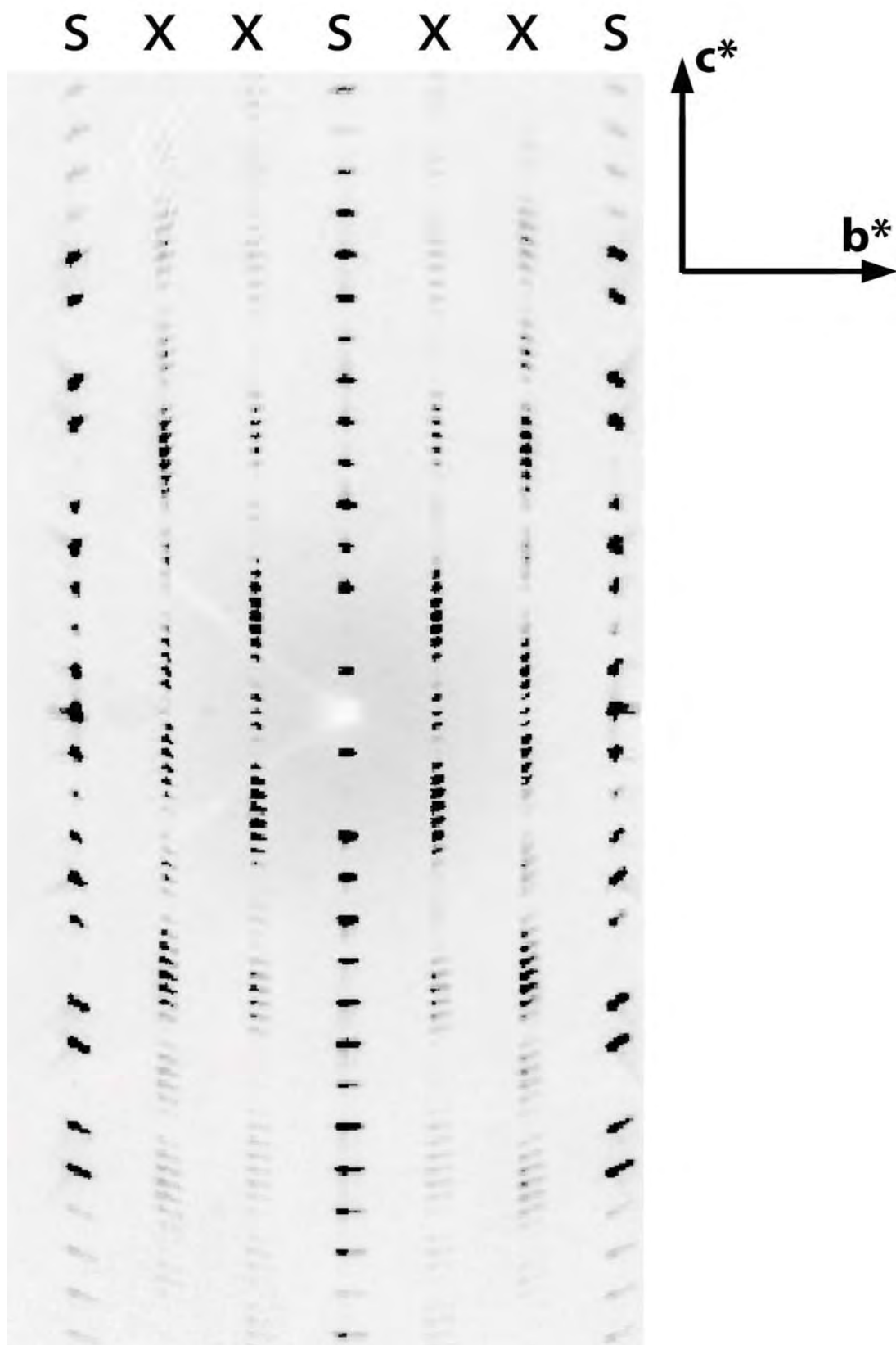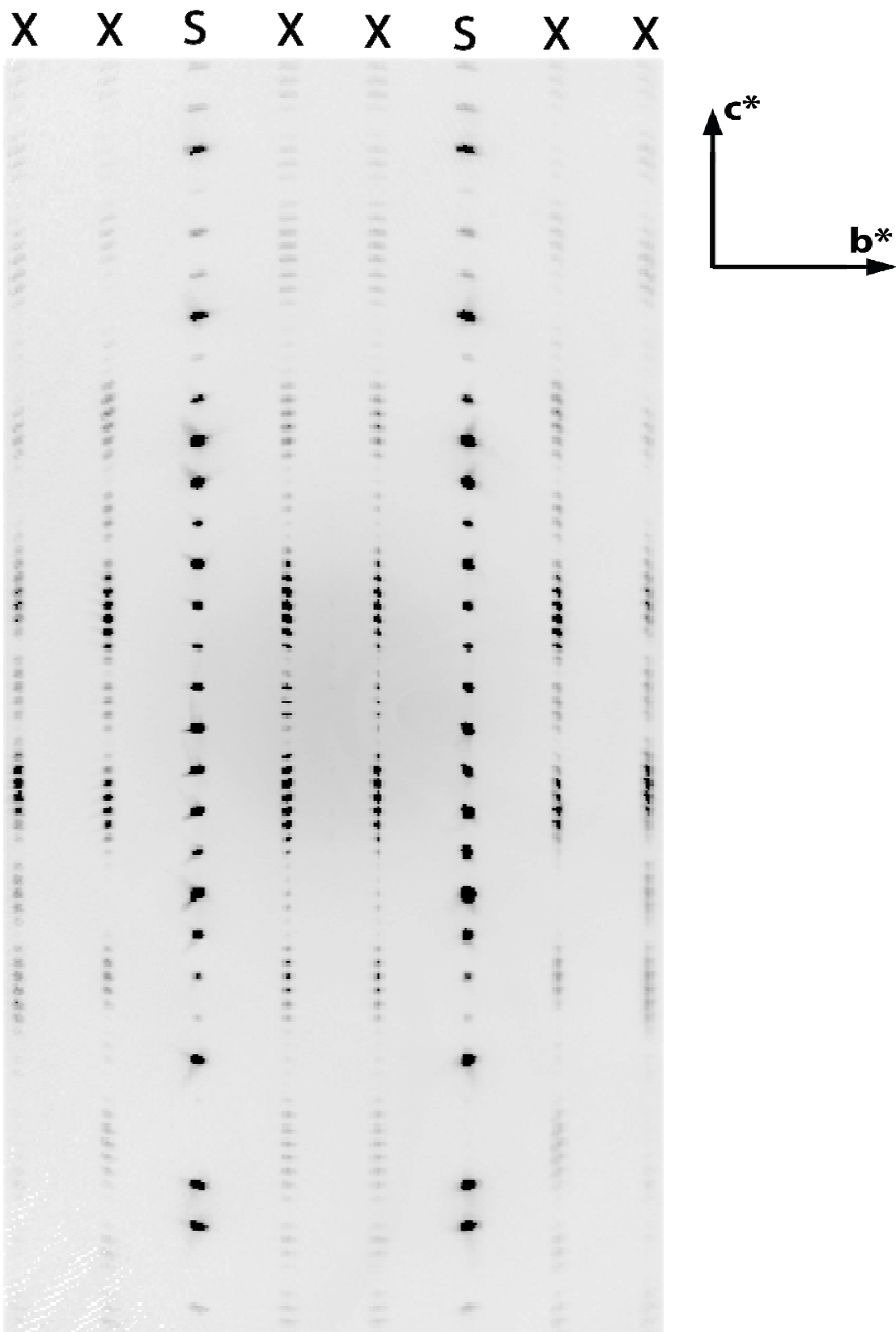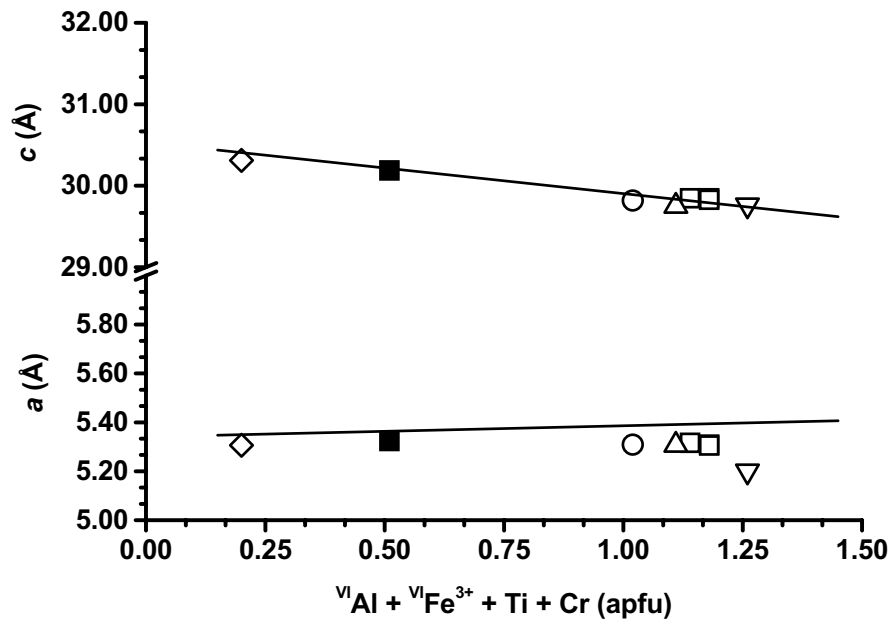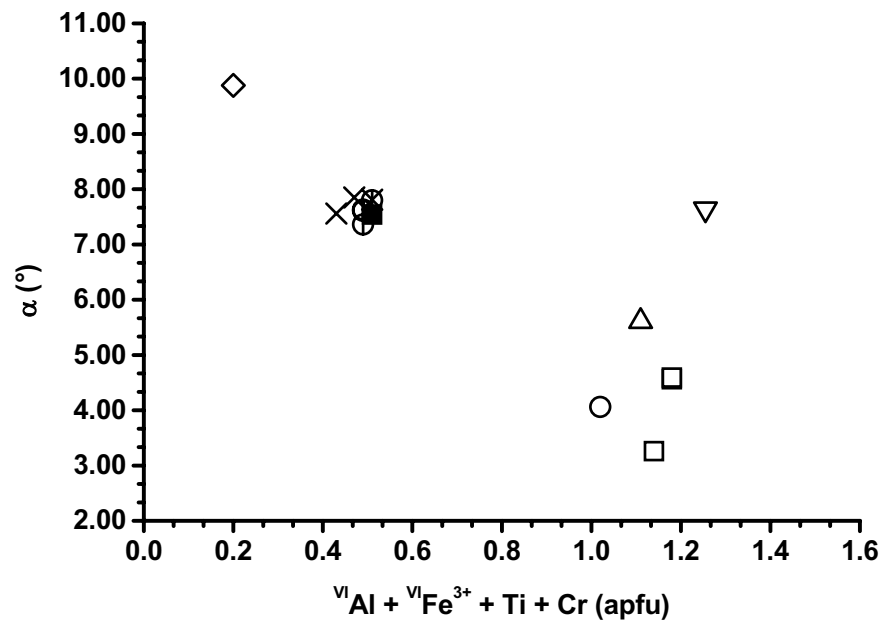
Figure 4d

Figure 5

Figure 6
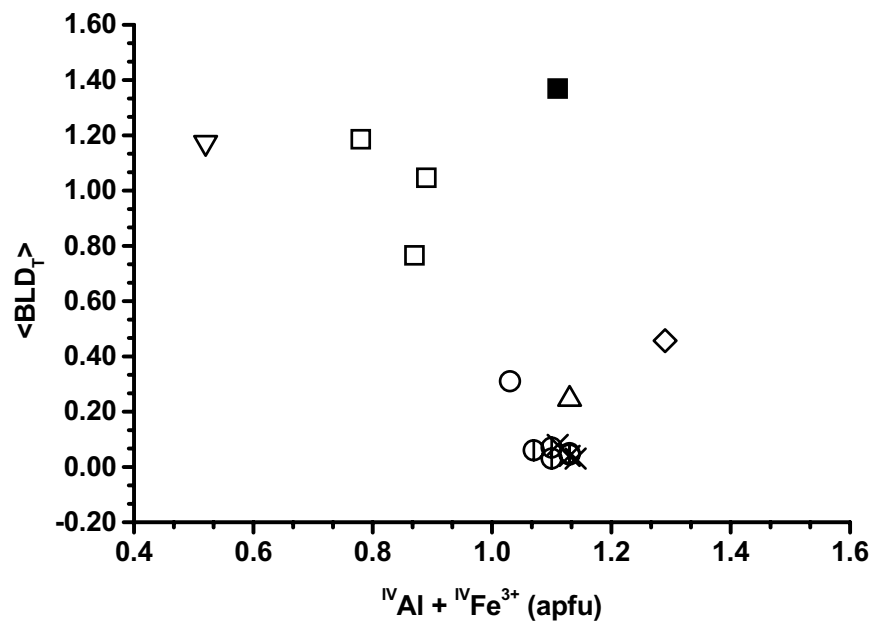
Figure 7

Table 1. Electron microprobe data (wt%) of the BU1_13 sample.

	3*T* polytype BU1_13	1*M* polytype BU1_1[†]	2*M*$_1$ polytype BU1_14[†]
SiO$_2$	38.7(2)	40(1)	38.2(2)
Al$_2$O$_3$	13.08(9)	13.7(4)	12.9(1)
MgO	20.4(2)	21.4(5)	20.4(1)
FeO	5.51(9)	5.6(1)	5.9(1)
TiO$_2$	4.8(1)	4.7(1)	5.0(1)
Cr$_2$O$_3$	0.90(7)	0.81(2)	0.63(4)
NiO	0.11(5)	0.09(3)	0.10(4)
MnO	0.03(3)	0.02(3)	0.03(2)
SrO	0.03(3)	b.d.l.	0.03(4)
ZnO	0.04(3)	b.d.l.	0.02(3)
ZrO$_2$	0.01(2)	b.d.l.	0.01(1)
K$_2$O	9.64(5)	9.9(2)	9.97(4)
Na$_2$O	0.29(1)	0.39(3)	0.26(3)
BaO	0.15(5)	0.25(3)	0.18(6)
CaO	n.d.	0.01(1)	0.00(1)
F	0.13(5)	0.5(1)	0.22(4)
Cl	0.01(1)	0.01(1)	0.01(1)
Total	93.8(3)	97(1)	93.9(3)
O = F	0.055		
O = Cl	0.002		
H$_2$O*	2.65		

Note: *H$_2$O value taken from Lacalamita et al. (2012); [†]from Lacalamita et al. (2012); n.d. = not determined; b.d.l. = below detection limit.

Table 2. Crystal, experimental and refinement data of the BU1_13 sample.

	BU1_13
Crystal size (mm^3)	0.58x0.32x0.02
Space group	$P3_112$
a (Å)	5.3235(3)
b (Å)	5.3235(3)
c (Å)	30.188(2)
Cell volume (Å^3)	740.9(1)
Z	3
Radiation	MoKa (0.7107 Å)
θ range for data collection	2 to 36°
Reflections collected	21581
Reflections unique	1359
$R_{merging}$ [$R_{(int)}$] (%)	4.62
Reflections used ($I>3\sigma(I)$)	1029
No. of refined parameters	116
Goof*	1.12
R_1[†] (%)	4.34
wR_2[‡] (%)	3.33
$\Delta\rho_{min}/\Delta\rho_{max}$ (e/Å^3)	-1.71/1.06

Notes:
*: Goodness-of-fit = $[\Sigma[w(F_o^2-F_c^2)^2]/(N\text{-p})]^{1/2}$, where N and p are the number of reflections and parameters, respectively.
[†]: $R_1 = \Sigma[|F_o| - |F_c|]/\Sigma|F_o|$.
[‡]: $wR_2 = [\Sigma[w(F_o-F_c)^2]/\Sigma[w(F_o)^2]]^{1/2}$; w = Chebyshev optimized weights.

Table 3. Crystallographic coordinates, occupancies, equivalent isotropic ($Å^2$) and anisotropic displacement parameters of the BU1_13 sample.

Site	Atom	x	y	z	Occupancy	$U_{iso/equiv}$	U_{11}	U_{22}	U_{33}	U_{23}	U_{13}	U_{12}
K	K^+	0.8894(2)	0.1106(2)	0.8333	1.022(3)	0.036(1)	0.0358(6)	0.0358(6)	0.0362(5)	-0.0009(7)	0.0037(7)	0.0183(8)
M1	Mg^{2+}	0.9041(4)	0.4523(2)	0	0.798(5)	0.011(1)	0.0015(6)	0.0087(6)	0.0191(9)	0.0017(3)	0	0.0007(3)
	Fe^{2+}				0.202(4)							
M2	Mg^{2+}	0.2277(4)	0.1138(2)	0	0.773(3)	0.015(1)	0.0158(7)	0.0091(5)	0.0147(5)	0.0010(6)	0	0.0016(4)
	Fe^{2+}				0.227(3)							
M3	Mg^{2+}	1.5772(4)	0.7886(2)	0	0.809(5)	0.0010(1)	0.0054(6)	0.0107(6)	0.0114(7)	0.0007(6)	0	0.0027(3)
	Fe^{2+}				0.191(4)							
T1	Si, Si^{4+}	0.2326(2)	0.7870(2)	0.90887(5)	1.009(8)	0.010(1)	0.0066(5)	0.0095(4)	0.0111(7)	0.0006(4)	0.0012(3)	0.0016(4)
T2	Si, Si^{4+}	0.5689(2)	0.4405(2)	0.90877(5)	0.995(8)	0.0010(1)	0.0084(5)	0.0109(5)	0.0152(8)	0.0010(3)	0.0005(3)	0.0087(4)
O1	O, O^{2-}	0.2361(6)	0.7845(7)	0.9640(2)	1.000(7)	0.010(2)	0.008(1)	0.009(1)	0.012(2)	-0.001(1)	0.0003(9)	0.003(1)
O2	O, O^{2-}	0.5694(6)	0.4466(7)	0.9633(2)	1.000(7)	0.012(3)	0.008(1)	0.015(2)	0.015(2)	0.0023(9)	0.0003(9)	0.0070(9)
O3	O, O^{2-}	0.3538(7)	0.113(1)	0.88946(9)	1.000(7)	0.019(2)	0.023(2)	0.015(1)	0.016(1)	-0.000(2)	-0.001(1)	0.007(2)
O4	O, O^{2-}	0.896(1)	0.5776(8)	0.88983(9)	1.000(7)	0.019(2)	0.013(1)	0.026(2)	0.015(1)	-0.003(1)	0.000(1)	0.008(2)
O5	O, O^{2-}	0.4315(9)	0.6516(8)	0.8894(1)	1.000(7)	0.020(3)	0.026(2)	0.023(2)	0.018(1)	0.003(1)	0.004(1)	0.018(1)
O6	O, O^{2-}	0.9017(7)	0.1165(7)	0.96606(6)	1.000(7)	0.011(2)	0.011(1)	0.008(1)	0.0131(7)	-0.003(1)	-0.004(1)	0.005(1)

Table 4. Selected bond distances (Å), mean atomic numbers (e⁻) of cation sites, tetrahedral and octahedral mean distances (Å) as determined by chemical determinations (EPMA) of the BU1_13 sample. The error for mean atomic numbers is ± 0.5 e⁻.

BU1_13			
T1-O1	1.664(5)	**M1-O1(x2)**	2.076(4)
T1-O3	1.629(5)	**M1-O2(x2)**	2.086(4)
T1-O4	1.671(5)	**M1-O6(x2)**	2.054(3)
T1-O5	1.658(5)	**<M1-O>**	2.072(6)
<T1-O>	1.656(10)		
		M2-O1(x2)	2.083(4)
T2-O2	1.647(6)	**M2-O2(x2)**	2.110(4)
T2-O3	1.641(4)	**M2-O6(x2)**	2.021(3)
T2-O4	1.617(5)	**<M2-O>**	2.071(6)
T2-O5	1.721(5)		
<T2-O>	1.657(10)	**M3-O1(x2)**	2.107(4)
<T-O>	1.657(14)	**M3-O2(x2)**	2.113(4)
<T-O> EPMA	1.663	**M3-O6(x2)**	2.016(3)
T e⁻ X-ref	14.03	**<M3-O>**	2.079(6)
T e⁻ EPMA	13.98		
		<M-O>	2.074(14)
		<M-O> EPMA	2.073
K-O3(x2)	2.991(3)	**e⁻ (M1) X-ref**	14.83
K-O4(x2)	3.002(3)	**e⁻ (M2) X-ref**	15.18
K-O5(x2)	2.970(3)	**e⁻ (M3) X-ref**	14.67
<K-O>inner	2.988(5)	**e⁻ (M1+M2+M3) X-ref**	44.68
		e⁻ (M1+M2+M3) EPMA	43.49
K-O3'(x2)	3.323(3)		
K-O4'(x2)	3.325(3)		
K-O5'(x2)	3.343(4)		
<K-O>outer	3.330(6)		
<K-O>	3.159(9)		
K e⁻ X-ref	19.42		
K e⁻ EPMA	18.18		

Table 5. Cation partitioning, mean atomic numbers (e⁻) of cation sites and mean interatomic distances (Å) as determined by structure refinement (X-ref) and chemical determinations (EPMA) for T and M sites of the BU1_13 sample. The error for mean atomic numbers is ± 0.5 e⁻.

Polytype	Site	Atoms per formula unit	e⁻ EPMA	e⁻ X-ref	Distance$_{EPMA}$	Distance$_{X-ref}$
3T						
	T1	$(Si_{0.72}Al_{0.26}Fe^{3+}_{0.02})$	13.98	14.13	1.663	1.656(10)
	T2	$(Si_{0.72}Al_{0.26}Fe^{3+}_{0.02})$	13.98	13.93	1.663	1.657(10)
	M1	$(Mg_{0.73}Fe^{2+}_{0.16}Al_{0.11})$	14.35	14.83	2.079	2.072(6)
	M2	$(Mg_{0.775}Fe^{2+}_{0.02}Fe^{3+}_{0.04}Ti_{0.135}Cr_{0.025}Ni_{0.005})$	14.57	15.18	2.070	2.071(6)
	M3	$(Mg_{0.775}Fe^{2+}_{0.02}Fe^{3+}_{0.04}Ti_{0.135}Cr_{0.025}Ni_{0.005})$	14.57	14.67	2.070	2.079(6)
1M, 2M₁[†]	M1	$(Mg_{0.76}Fe^{2+}_{0.16}Al_{0.08})$				
	M2	$(Mg_{0.775}Fe^{2+}_{0.02}Fe^{3+}_{0.04}Ti_{0.13}Al_{0.005}Cr^{3+}_{0.025}Ni_{0.005})$				

Note: [†]from Lacalamita et al. (2012)

Table 6. Distortional parameters comparison between 1*M*-, 2*M*₁- and 3*T*-BU1 crystals.

	3*T* polytype		1*M* polytype	2*M*₁ polytype	
	BU1_13		**BU1_1**[†]	**BU1_14**[†]	
	T1	**T2**	**T**	**T1**	**T2**
BLD$_T$	0.81	1.93	0.08	0.06	0.04
Volume$_T$ [Å³]	2.324	2.330	2.336	2.329	2.329
TQE	1.001	0.999	1.000	1.000	1.000
TAV	2.8	6.1	1.6	1.4	1.5
τ [°]	110.7	110.4	110.5	110.5	110.6
t $_{tet}$ [Å]	2.237		2.239	2.262	
α[°]	7.54		7.81	7.63	
Δz [Å]	0.013		0.006	0.011	
D.M. [Å]	0.502		0.516	0.507	
	M1	**M2**	**M3**	**M1** **M2**	**M1** **M2**
ψ$_M$ [°]	58.02	58.14	58.14	59.11 58.84	59.03 58.80
BLD$_M$	0.58	1.60	1.35	0.72 1.76	0.78 1.80
ELD$_M$	4.89	4.88	5.03	5.25 4.94	5.16 4.89
Volume$_M$ [Å]	11.68	11.66	11.78	11.85 11.60	11.84 11.62
OQE$_M$	1.010	1.011	1.006	1.012 1.011	1.012 1.011
OAV$_M$	34.5	35.6	37.0	39.7 35.9	38.2 35.3
e$_u$/e$_s$	1.103	1.096	1.106	1.111 1.104	1.109 1.103
Shift$_M$	0.008	0.059	0.061	0.039	0.054
t $_{oct}$ [Å]	2.146		2.140	2.143	
t $_{int}$ [Å]	3.395		3.406	3.395	
Δ$_{K-O}$ [Å]	0.342		0.355	0.347	
t $_{K-O4}$ [Å]	4.007		3.957	3.994	

Note: [†]from Lacalamita et al. (2012); t$_{tet}$: tetrahedral sheet thickness calculated from z coordinates of basal and apical O atoms; TQE: tetrahedral quadratic elongation (Robinson et al. 1971); TAV: tetrahedral angle variance (Robinson et al. 1971); τ: tetrahedral flattening angle; α: tetrahedral rotation angle (Hazen and Burnham 1973); Δz: departure from complanarity of the basal O atoms (Güven 1971); D.M.: dimensional misfit between tetrahedral and octahedral sheets (Toraya 1981); ψ: octahedral flattening angles (Donnay et al. 1964a, 1964b); BLD: bond-length distortions (Renner and Lehmann 1986); ELD: edge-length distortion (Renner and Lehmann 1986) OQE: octahedral quadratic elongation (Robinson et al. 1971); OAV: octahedral angle variance (Robinson et al. 1971); e$_u$, e$_s$: mean lengths of unshared and shared edges, respectively (Toraya 1981); Shift$_M$ off-center shift of the M cation calculated using the IVTON software (Balic Zunic and Vickovic 1996); t$_{oct}$: octahedral sheet thickness (Toraya 1981); t$_{int}$ calculated from the z coordinates of basal O atoms; Δ$_{K-O}$ = <K-O>$_{outer}$-<K-O>$_{inner}$; t$_{K-O4}$: projection of K-O4 distance along c*. Errors on distortion parameters, estimated by varying the refined positional parameters within one standard deviation, are in the following ranges: < 0.5% for volumes, thicknesses, projected bond lengths, shift; 0.1-13% for angles, bond/edge lengths distortions, sheet corrugations, D.M., Δ$_{K-O.}$